Applied Mathematical Modelling 97 (2021) 821–838

Contents lists available at ScienceDirect

Applied Mathematical Modelling

journal homepage: www.elsevier.com/locate/apm

Modelling melting and grain destruction phenomena during globular equiaxed solidification

Haijie Zhang[a], Menghuai Wu[a,*], Peter Schumacher[b], Christian M.G. Rodrigues[a], Andreas Ludwig[a], Abdellah Kharicha[a]

[a] Chair for Simulation and Modeling of Metallurgy Processes, Department of Metallurgy, University of Leoben, Franz-Jose-Str. 18, Leoben A-8700, Austria
[b] Chair of Casting Research, Department of Metallurgy, University of Leoben, Leoben A-8700 , Austria

ARTICLE INFO

Article history:
Received 18 February 2021
Revised 14 April 2021
Accepted 28 April 2021
Available online 11 May 2021

Keywords:
Melting
Solidification
Nucleation
Macrosegregation
Modelling

ABSTRACT

Melting or re-melting accompanies solidification in many technical castings. For example, during ingot casting, some crystal fragments or equiaxed grains can enter the superheated region and re-melt, while solidification continues in other regions. Solidification and remelting occurring simultaneously at different locations present an important species/energy transport mechanism, which impacts the structural/compositional homogeneity of the castings. The re-melting is typically understood as a reduction in the equiaxed grain size, but it can also lead to the destruction (disappearance) of equiaxed grains. Existing process-based models cannot treat the solidification/melting by considering both grain nucleation and destruction properly. Therefore, a new model is proposed based on a two-phase volume-average approach. In this model, nucleation of equiaxed grains occurs when inoculants (free growth sites) are activated by undercooling, while destruction of equiaxed grains occurs only when the equiaxed grains are completely re-melted by superheating. The mass, momentum, species, and enthalpy conservation equations are solved for the solidification/melting. The transport equations for the number densities of equiaxed grains and inoculants are calculated separately. A test casting (Al–7 wt.% Si) is calculated to illustrate the modelling features. This study improves understanding of grain melting and grain destruction as well as their impact on the as-solidified structure.

1. Introduction

The melting or re-melting of equiaxed grains is an important phenomenon, which accompanies the solidification process in many technical castings. Melting and solidification can occur simultaneously or alternately at different locations of the casting domain. For example, during ingot casting, some crystal fragments or equiaxed grains can move and enter the superheated region and re-melt, while solidification continues in other regions. In practice, two conditions can lead to re-melting: an increase in the local temperature and a change in the local solute concentration [1–3]. Thermo-solutal

* Corresponding author.
E-mail address: menghuai.wu@unileoben.ac.at (M. Wu).

https://doi.org/10.1016/j.apm.2021.04.024

and/or forced convections are mainly responsible for these processes [4,5]. It was experimentally confirmed that grain nucleation, solidification, transport, re-melting, and destruction can occur simultaneously [5,6]. These simultaneous solidification/melting processes together with grain migration provide an important species/energy transport mechanism, impact the final as-formed structure, and influence the heterogeneity (macrosegregation) of castings.

While knowledge about nucleation and solidification appears to be well established [7,8], research on melting and grain destruction lags greatly behind the rest of the field. Based on published work [1,2,9–11], melting is not simply 'inverse solidification'. Complex kinetics that breaks the solidification/melting symmetry involve solute partitioning and solute redistribution, which can consistently update the grain morphology in the mushy zone. A temperature gradient zone melting experiment was performed to investigate the melting and re-solidification of an Al–Cu alloy under a stationary temperature gradient [2,12]. Melt convection and grain transport were not a/the focus of that experiment.

Melting experiments under natural convection condition were also performed [13–15]. By melting organic materials or metals in a rectangular enclosure vertically from one side, the motion and shape of the solid-liquid interface was tracked and analysed. These studies focused on the melt convection and its impact on the profile of the melting front, while grain transport was not explicitly discussed. However, the experimentally measured temperature information does imply that transport of crystal fragments and re-solidification could accompany the melting process as well. The transport, re-melting, and annihilation (destruction) of equiaxed grains by melt convection appears to be evidenced by Rerko et al. [16] in a grain-refinement Al–10 wt.% Cu solidification experiment. The grain size in the top-cooled ingots was approximately 3 times larger than that in the bottom-cooled ones. This difference was interpreted to be due to advection of nucleated grains and re-melting. For the top-cooled ingots, the cold solute-segregated melt descended and brought the equiaxed grains to warmer areas where some of them melted, leaving fewer equiaxed grains in the upper region to grow into a large size.

In the past decades, some efforts have been made in modelling the melting process [17]. Most simulations [18,19] focused on the melting of pure substance under natural/forced convection. The effect of thermo-solutal convection and the influence of solute transport on alloy solidification were investigated by Voller et al. [20] based on the enthalpy–porosity model. This model can be easily extended for the melting of alloys, but it is limited to rigid solid structures, such as eutectics and columnar dendrites. Similar work was done by Kumar et al. [11]. The cellular automaton (CA) method has also been used to simulate the melting and solidification of equiaxed grains, where solute redistribution during the phase transformation was calculated [21]. Once again, solid transport was not considered. The most promising model is the multiphase volume-average model [4,22–24] because it provides the flexibility to treat grain nucleation, liquid convection, grain transport and sedimentation, solute redistribution, and different growth kinetics during solidification/melting of equiaxed grains and columnar dendrites. The importance of grain destruction was addressed [24–27], but the proposed models for melting were greatly simplified, i.e. the grain number density was set to zero as soon as grains were advected into the superheated region.

In the current paper, a new model for treating melting and grain destruction during alloy solidification is proposed based on a two-phase volume-average approach. Both nucleation and destruction of equiaxed grains are considered. The mass, momentum, species, and enthalpy conservation equations are solved for globular equiaxed solidification/melting. The transports of the number densities of equiaxed grains and inoculants (free growth sites) are calculated individually. The modelling features are verified based on simulations of an Al-casting (Al–7 wt.% Si).

2. Model description (a two-phase model)

The fundamentals of volume-average-based solidification models can be found elsewhere [25,28,29]. In the current paper, the model is extended to cover the re-melting and destruction of equiaxed grains. It is well known that most alloys solidify into a mixed columnar–equiaxed structure. To focus on grain re-melting and destruction, here a two-phase globular equiaxed solidification model is used. The two phases are the liquid phase and solid phase (equiaxed grains). The volume fractions of the two phases always sum to 1.0, i.e. $f_\ell + f_e = 1$. The morphology of equiaxed grains is assumed to be spherical. Heterogeneous nucleation of equiaxed grains occurs by activating inoculants, i.e. free growth sites, when a necessary undercooling is achieved. Growth of the grains is governed by diffusion. A thermodynamic equilibrium applies at the solid–liquid interface, and the concentration difference between the thermodynamic equilibrium concentration of the liquid melt at the solid–liquid interface and the volume-averaged liquid concentration is the driving force for grain growth. The re-melting process includes two steps: reduction in the grain size (melting) and the destruction of the grain (disappearance). Re-melting occurs only when the equiaxed grains are exposed to the superheated melt. The reduction in the grain size is also governed by diffusion. Destruction of the grain occurs only when the grain is completely re-melted. It is assumed that the inoculant, on which the original equiaxed grain nucleated, is released after re-melting. This means that one re-melted/disappeared equiaxed grain will turn into one inoculant, which is reserved as a future potential nucleation (free growth) site. Therefore, the total number of grains and inoculants in the casting domain is conserved.

2.1. Transport of equiaxed grains and inoculants

The velocities of the melt and solid phase (equiaxed grains) are known by solving the Navier–Stokes equations ($\vec{u}_\ell$ and $\vec{u}_{eq}$, respectively). The motion of inoculants follows the velocity of the melt [28]. The transport equations for the number

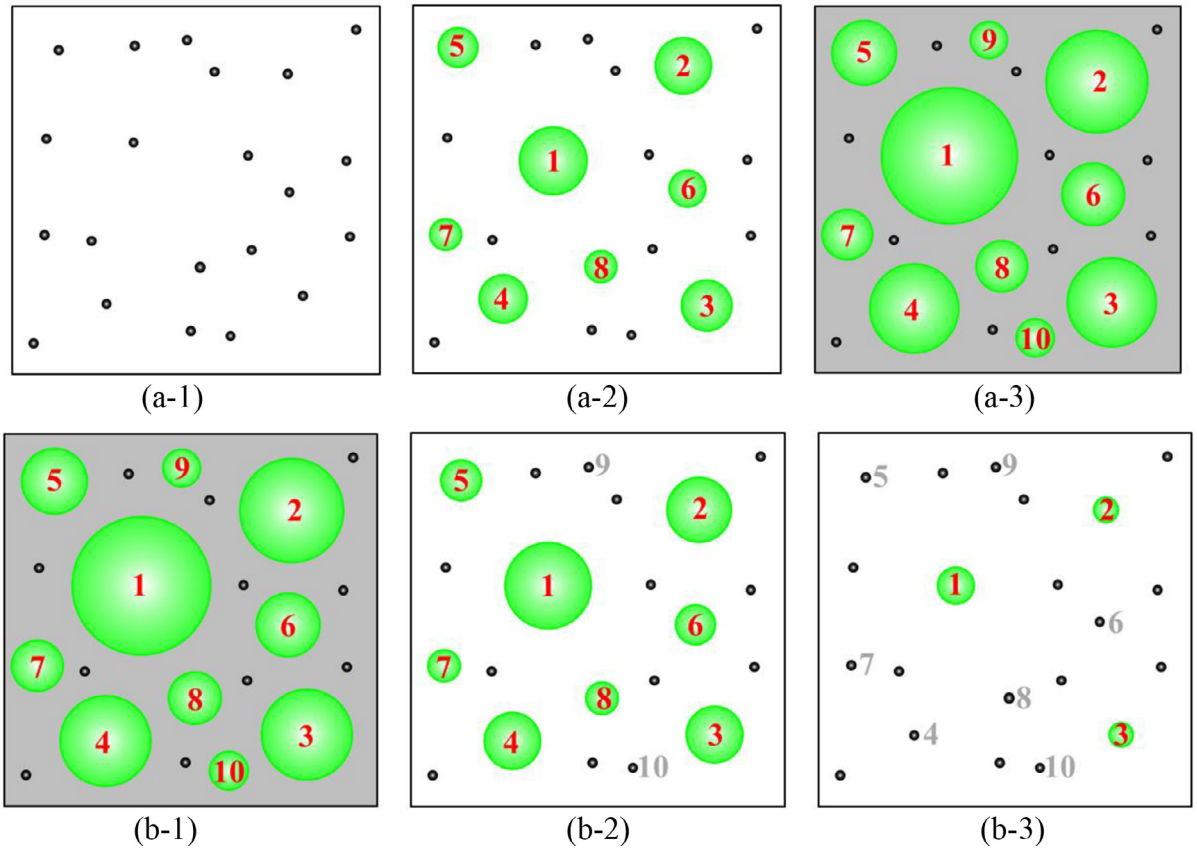

Fig. 1. Schematic of (a) the nucleation and grain growth and (b) the re-melting and grain destruction processes. The black dots denote the inoculants, the green spheres indicate the equiaxed grains, and the grey background indicates the eutectic phase. All grains are numbered from 1 to 10.

densities of equiaxed grains and inoculants are

$$\frac{\partial}{\partial t} n_{\mathrm{eq}} + \nabla \cdot \left(\vec{u}_{\mathrm{eq}}\, n_{\mathrm{eq}} \right) = \dot{n}, \tag{1}$$

$$\frac{\partial}{\partial t} n_{\mathrm{in}} + \nabla \cdot \left(\vec{u}_{\ell}\, n_{\mathrm{in}} \right) = -\dot{n}, \tag{2}$$

where n_{in} and n_{eq} are the number densities of the inoculants and equiaxed grains, respectively; $\dot{n}$ is the nucleation/destruction rate. The drag force between the liquid melt the solid equiaxed grains is approximated by the Kozeny–Carman equation for $f_{\mathrm{e}} \langle\ 0.7$ and the Blake–Kozeny equation for $f_{\mathrm{e}} \geq 0.7$ [30]. The interactions between neighbouring equiaxed grains are modelled by the effective viscosity. A mixing rule was employed to estimate the viscosity of the equiaxed phase, which can be calculated via $\mu_{\mathrm{e}} = \frac{\mu_{\ell}}{f_{\mathrm{e}}}((1 - f_{\mathrm{e}}/f_{\mathrm{e}}^{\mathrm{c}})^{-2.5 \cdot f_{\mathrm{e}}^{\mathrm{c}}} - (1 - f_{\mathrm{e}}))$ [26]. To deal with the hydrodynamic interaction between phases, the equiaxed grains are assumed to have envelopes and their volume fractions are indicated by $f_{\mathrm{e}}^{\mathrm{Env}}$. The volume fraction of grain envelope ($f_{\mathrm{e}}^{\mathrm{Env}}$) is related to the volume fraction of solid (f_{e}) through $f_{\mathrm{si}} = f_{\mathrm{e}}/f_{\mathrm{e}}^{\mathrm{Env}}$, where f_{si} is the volume ratio of the solid grain to the equiaxed grain envelope. In this study, f_{si} is set as a constant value (0.235). When $f_{\mathrm{e}}^{\mathrm{Env}}$ is beyond the packing limit ($f_{\mathrm{e}}^{\mathrm{c}} = 0.637$), the equiaxed phase becomes a rigid porous medium, through which the liquid is still able to penetrate via the voids between the closely packed grains. Further discussion on "envelope concept" is made in Section 5.4.

2.2. Heterogeneous nucleation and solidification

The nucleation sequence during the solidification process is schematically shown in Fig. 1(a). Inoculants exist in the parent melt (Fig. 1 (a-1)). With sufficient undercooling, they are activated to become equiaxed grains (Fig. 1 (a-2)). The undercooling for activating an inoculant depends on its size [31]. Consequently, the number of inoculants in the melt gradually decreases. The final solidification structure of the sample may consist of a eutectic phase, primary equiaxed grains with various sizes, and inactivated inoculants embedded in the eutectic phase (Fig. 1 (a-3)). It is well known that certain alloying

and impurity elements can poison the inoculants (grain refiners) and therefore adversely affect grain refinement [32]. The poisoning effect is ignored in the current study.

A continuous nucleation formulation (Gaussian distribution), as proposed by Rappaz and Gandin [33,34], has been widely used to model heterogenous grain nucleation during solidification [35,36]. A Gaussian distribution can be used as an approximation of a log normal distribution if the inoculant diameter is relatively large [31,37]. The originally proposed Gaussian distribution assumed that there were a certain amount of free nucleation sites (inoculants) in the melt ($n_{\max}$), and the free nucleation sites were uniformly distributed in the casting. This assumption is inconsistent with practical solidification conditions. An uneven distribution of inoculants will be achieved owing to nucleation and/or advection. The number density of the inoculant gradually decreases as nucleation occurs. In the current paper, the inoculants and equiaxed grains are distinguished and quantified by their number densities (n_{in} and n_{eq}, respectively). The number density of the inoculants can be transported, and it changes depending on local nucleation or grain destruction. The original continuous nucleation formulation of Rappaz and Gandin [33,34] is slightly updated by replacing $n_{\max}$ with the number density of the available inoculants n_{in} [28,38]:

$$\frac{dn_{\text{eq}}}{d(\Delta T)} = \frac{n_{\text{in}}}{\sqrt{2\pi}\cdot\Delta T_\sigma}\cdot \mathrm{e}^{-\frac{1}{2}\cdot\left(\frac{\Delta T-\Delta T_{\text{N}}}{\Delta T_\sigma}\right)^2}, \tag{3}$$

where ΔT is the undercooling, and ΔT_σ and ΔT_{N} are the standard deviation and mean of the Gaussian distribution of nucleation undercooling. The local undercooling can be calculated by

$$\frac{D(\Delta T)}{Dt} = \frac{\partial \Delta T}{\partial t} + m\cdot \vec{u}_\ell \cdot\nabla c_\ell - \vec{u}_\ell \cdot\nabla T_\ell, \tag{4}$$

where t is time, m is the liquidus slope from the phase diagram, T_ℓ and ∇T_ℓ are the temperature and its gradient of the liquid phase, c_ℓ and ∇c_ℓ are the volume-averaged concentration and its gradient of the melt. ΔT can be calculated via $\Delta T = T_f + m\cdot c_\ell - T$, in which T_f it the melting point of solvent. The nucleation rate, $\dot{n} = D(n_{\text{eq}})/Dt$, is calculated by

$$\dot{n} = \frac{D(\Delta T)}{Dt}\cdot\frac{dn_{\text{eq}}}{d(\Delta T)}. \tag{5}$$

Note that groups of inoculants with different sizes could be followed individually [39]. However, it would require massive computational resources. Therefore, all inoculants are assumed to have the same size, but they are activated as nuclei at different undercoolings, statistically following the Gaussian distribution. The solidification rate, i.e. the rate of mass transfer from the liquid to the equiaxed solid ($M_{\ell \text{e}}$), is calculated by

$$M_{\ell \text{e}} = v_{\text{R}_\text{e}}\cdot\left(n_{\text{eq}}\cdot\pi d_{\text{e}}^2\right)\cdot\rho_{\text{e}}\cdot f_\ell, \tag{6}$$

with

$$v_{\text{Re}} = \frac{D_\ell}{l_\ell}\cdot\frac{(c_\ell^* - c_\ell)}{(1-k)c_\ell^*} + \frac{D_{\text{e}}}{l_{\text{e}}}\cdot\frac{(c_{\text{e}}^* - c_{\text{e}})}{(1-k)c_\ell^*}, \tag{7}$$

where v_{Re} is the grain growth speed, d_{e} is the average grain diameter, ρ_{e} is the density of the equiaxed phase, k is the solute partition coefficient, c_ℓ^* is the thermodynamic equilibrium concentration of the liquid, D_ℓ and D_{e} are the solute diffusion coefficients, l_ℓ (= d_{e}) and l_{e} (= $d_{\text{e}}/6$) are the corresponding diffusion lengths in the liquid melt and solid grains, respectively.

2.3. Melting and grain destruction

The melting/grain-destruction process is schematically shown in Fig. 1(b). The primary material includes the as-cast structure, i.e. eutectic phase, equiaxed grains and some inactivated inoculants (Fig. 1 (b-1)). As the temperature increases, the eutectic phase begins melting first. This process releases the embedded equiaxed grains and inactivated inoculants, and they are free to move again. With further re-melting of the equiaxed grains, their sizes decrease, which is followed by grain destruction (Fig. 1 (b-2)). The two smallest equiaxed grains (numbered 9–10) are completely melted/destroyed; thus, they are turned into inoculants. At a later stage, Fig. 1 (b-3), most grains are melted/destroyed, and there are only three equiaxed grains (1–3) that remain.

Although the volume-average model computes only one average grain size (d_{e}), the equiaxed grains are assumed to follow a lognormal size distribution (Appendix A).

$$\frac{d(n_{\text{eq}})}{d(x)} = \frac{n_{\text{eq}}}{\sqrt{2\pi}\sigma x}e^{-\frac{1}{2}\left(\frac{\ln(x)-\ln(\hat{d}_{\text{e}})}{\sigma}\right)^2}, \tag{8}$$

where

$$1 = \int_0^\infty \frac{1}{\sqrt{2\pi}\sigma x}e^{-\frac{1}{2}\left(\frac{\ln(x)-\ln(\hat{d}_{\text{e}})}{\sigma}\right)^2} d(x), \tag{9}$$

where σ is the geometric standard deviation of the lognormal distribution, the dummy variable (x) corresponds the grain diameter of different size classes, and $\hat{d}_{\text{e}}$ is the geometric mean. Note that the geometrical mean of the grain size ($\hat{d}_{\text{e}}$) is

different from the volume-averaged grain size (d_e). However, it is assumed that their variation during melting follows a similar trend, i.e. $d(\hat{d}_e)/dt \approx d(d_e)/dt$, which can be estimated by v_{Re}. A critical value of the grain size ($d_{e,critical}$) is introduced. When a size class of equiaxed grains is melted to smaller than $d_{e,critical}$, it will be eliminated from n_{eq}. Therefore, the grain destruction rate, $\dot{n} = dn_{eq}/dt$, is calculated by

$$\dot{n} = v_{Re} \cdot \left.\frac{d(n_{eq})}{d(x)}\right|_{x=d_{e,critical}}. \tag{10}$$

Because melting is assumed to be governed by diffusion, Eq. (7) is valid for calculating v_{Re}. During melting, the equilibrium concentrations (c_ℓ^* and c_e^*) are lower than the volume-averaged concentrations (c_ℓ and c_e); therefore, a negative value of v_{Re} is obtained. Because dn_{eq}/dx is always positive, if v_{Re} is negative, the $\dot{n}$ calculated by Eq. (10) is also negative. The melting rate, i.e. the rate of mass transfer from the equiaxed to the liquid ($M_{\ell e}$), is calculated by

$$M_{\ell e} = v_{R_e} \cdot \left(n_{eq} \cdot \pi d_e^2\right) \cdot \rho_\ell. \tag{11}$$

Because no geometrical impingement factor is necessary for melting, Eq. (11) differs from Eq. (6). The energy, momentum, and species transfer between the liquid and the equiaxed solid during the solidification/melting process can be found in our previous papers [23,28]. Eutectic reaction/melting occurs when the temperature decreases/increases to the eutectic isotherm. In the current model, the release/absorption of latent heat during the eutectic reaction/melting is approximated with the temperature compensation method. The remaining liquid after the eutectic reaction is considered as eutectic phase. To analyse the macrosegregation, a mixture concentration is defined: $c_{mix} = (c_\ell \cdot \rho_\ell \cdot f_\ell + c_e \cdot \rho_e \cdot f_e)/(\rho_\ell \cdot f_\ell + \rho_e \cdot f_e)$. The macrosegregation intensity is characterised by its index: $c_{mix}^{index} = (c_{mix} - c_0)/c_0 \cdot 100\%$.

2.4. Solution procedures/strategy

The current model was implemented in the commercial Ansys Fluent software (version 17.1), which uses a control-volume method. The solver in Ansys Fluent provides a platform to solve the global transport equations. In addition, it provides flexibility (open program interface) in defining the exchange/source terms for the transport equations, and even allows modification of the solution procedure [29]. One numerical constraint is applied, i.e. the minimum value of $n_{in}$and n_{eq} was enforced to be 10^7 m^{-3}. It is difficult for Eqs. (1) and (2) to converge when the transport quantity becomes too small in comparison to its source term. All transport equations were solved in an iterative manner. For each time step, up to 20 iterations were used to decrease the normalised residuals of the phase fraction, velocity components, pressure, and species below 10^{-4} and enthalpy quantities below 10^{-7}. The time step that ensures a high accuracy solution must be determined empirically by test simulations. In this study, all calculations were conducted with a time step of 0.001 s. Conservation of the species and number densities of the grains and inoculants is guaranteed in the system.

3. Configuration of test simulation cases

A 2D geometry (60width × 80height mm^2) was meshed to a size of 1.0 × 1.0 mm^2, and an Al–7 wt.% Si alloy was calculated. The Al–Si binary phase diagram was linearised, and the liquidus slope (m) and the solute partition coefficient (k) were assumed to be constant. A no-slip boundary condition was assumed to be valid on the domain surface. Before the start of the simulation, the domain was set to be uniform in concentration ($c_0 = 0.07$) and temperature ($T_0 = 900$ K). As the initial condition, the minimum value was assigned for n_{eq} (10^7 m^{-3}), while a very large value was assigned for n_{in} (2.0×10^{10} m^{-3}). The material properties and other parameters are summarised in Table I.

Two simulation cases were designed. Case I was used to check the model implementation. The sample was solidified and re-melted under purely diffusive condition. No flow and grain sedimentation were considered. A Dirichlet boundary condition was applied on four walls. The corresponding temperature profiles can be found in Fig. 2(a). The sample was cooled to below eutectic temperature in stage A, heated to over the melting point in stage B, and then cooled again in stage C. To simplify case I, the latent heat was not considered, and an extreme large conductivity (10^7 W·m^{-1}·K^{-1}) was used for both the liquid and equiaxed phases. Therefore, the entire sample had a nearly uniform temperature during the cooling/heating processes.

Case II was similar to a practical solidification/melting process, where thermo-solutal convection and grain sedimentation were considered. In case II (stage A), only the right wall was cooled, following the temperature profile shown in Fig. 2(b). The other three walls were adiabatic. The as-solidified phase distribution of case II (stage A) was used as the initial condition for case II (stage B). The left wall was heated again, following the temperature profile of Fig. 2(c), while other walls were adiabatic. In case II, the true physical values of latent heat and heat conductivities of the alloy were used.

4. Simulation results

4.1. Case I: solidification and melting under purely diffusive conditions

The solidification/melting sequence of the sample is shown in Fig. 3. All solidification quantities were taken from the domain centre. The calculated T followed the pre-defined temperature profiles exactly (Fig. 3(a)). The calculated undercooling (ΔT) is plotted in Fig. 3(b). At the beginning of stage A, the melt was superheated. With the decrease in T, the melt

Table 1
Material properties of Al–7 wt.% Si and other parameters [40–42].

Properties/parameters	Symbol	Units	Values
Thermophysical			
Specific heat	c_p^{ℓ}, c_p^{e}	$J{\cdot}kg^{-1}{\cdot}K^{-1}$	1140.0
Latent heat	Δh_f	$J{\cdot}kg^{-1}$	4.0×10^{5}
Diffusion coefficient (liquid)	D_ℓ	$m^2{\cdot}s^{-1}$	6.5×10^{-9}
Diffusion coefficient (solid)	D_e	$m^2{\cdot}s^{-1}$	1.0×10^{-12}
Thermal conductivity (liquid)	k_p^{ℓ}	$W{\cdot}m^{-1}{\cdot}K^{-1}$	76.7
Thermal conductivity (solid)	k_p^{e}	$W{\cdot}m^{-1}{\cdot}K^{-1}$	185.0
Liquid thermal expansion coefficient	β_T	K^{-1}	-1.85×10^{-4}
Liquid solutal expansion coefficient	β_c	$wt.\%^{-1}$	1.3×10^{-3}
Density	ρ_ℓ,ρ_e	$kg{\cdot}m^{-3}$	2535.0
Density difference (Boussinesq)	$\Delta\rho(=\rho_e-\rho_\ell)$	$kg{\cdot}m^{-3}$	137.0
Viscosity	μ_ℓ	$kg{\cdot}m^{-1}{\cdot}s^{-1}$	2.52×10^{-3}
Thermodynamic			
Eutectic temperature	T_{eu}	K	850.0
Liquidus slope	m	$K{\cdot}wt.\%^{-1}$	−6.62
Equilibrium partition coefficient	k	–	0.13
Primary dendrite arm spacing	λ_1	m	3.0×10^{-4}
Secondary dendrite arm spacing	λ_2	m	5.0×10^{-5}
Gibbs–Thomson coefficient	Γ	m·K	2.4×10^{-7}
Melting point of solvent	T_f	K	933.4
Nucleation/Destruction			
Standard deviation for nucleation	ΔT_σ	K	0.5
Mean nucleation undercooling	ΔT_N	K	4.0
Standard deviation for destruction	σ	–	0.873
Critical diameter for grain destruction	$d_{e,critical}$	m	3.0×10^{-5}
Other			
Initial concentration	c_0	wt.%	7.0
Initial temperature	T_0	K	900.0
Initial number density of equiaxed grains	$n_{eq,0}$	m^{-3}	1.0×10^{7}
Initial number density of inoculants	$n_{in,0}$	m^{-3}	2.0×10^{10}
Cooling/heating rate	R	$K{\cdot}s^{-1}$	± 0.25

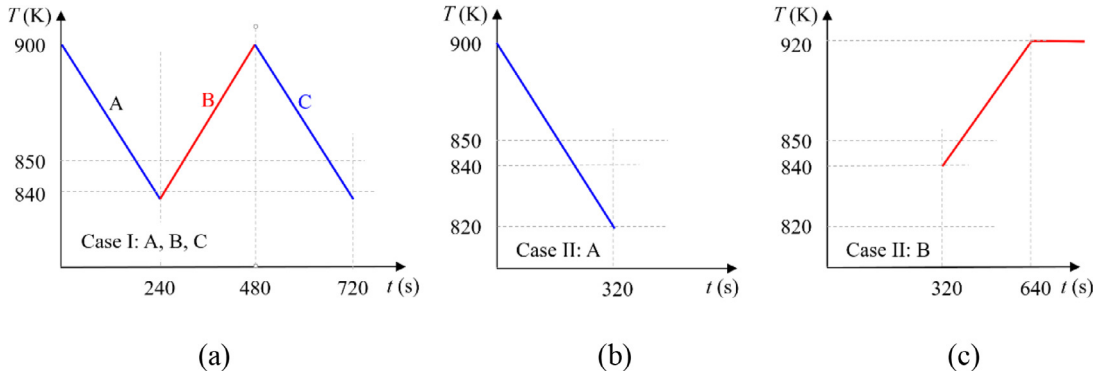

Fig. 2. Dirichlet thermal boundary conditions for different test simulation cases. (a) Case I: cooling and heating in different stages (A–C) equally from all walls; (b) case II (stage A): cooling from the right wall only; and (c) case II (stage B): heating from the left wall only. The heating/cooling rate had the same magnitude: 0.25 $K{\cdot}s^{-1}$.

became undercooled at 30 s. Because of the undercooling, inoculants started to be activated as nuclei. As shown in Fig. 3(c), a number of inoculants were consumed, and the same number of equiaxed grains were generated. The formed grains grew in the undercooled melt. This can be seen through the positive $M_{\ell e}$ in Fig. 3(d). The direct outcomes of nucleation and solidification are an increase in f_e and a decrease in f_ℓ (Fig. 3(e)). The calculated volume-averaged diameter of the equiaxed grains, $d_e = \sqrt[3]{6f_e/\pi n_{eq}}$, is plotted in Fig. 3(f). d_e exhibited an increasing trend in stage A, except for a singular point at around 60 s. This singular point was caused by an instantaneous nucleation event. A sudden increase in n_{eq} will reduce the volume-averaged grain diameter (d_e). From Fig. 3(c), it can be seen the nuclei mainly formed during the early stage of solidification (30–85 s). After 85 s, there was almost no new nucleation. Only the formed equiaxed grains continued to grow. The mass transfer between the liquid and the equiaxed phases ($M_{\ell e}$) terminated when the temperature was below T_{eu}. At the end of stage A, the sample solidified with $n_{eq} = 1.4 \times 10^{10}$ m^{-3}, $n_{in} = 5.6 \times 10^{9}$ m^{-3}, $f_e = 0.48$, $f_{eut} = 0.52$, and $d_e = 4.0 \times 10^{-4}$ m.

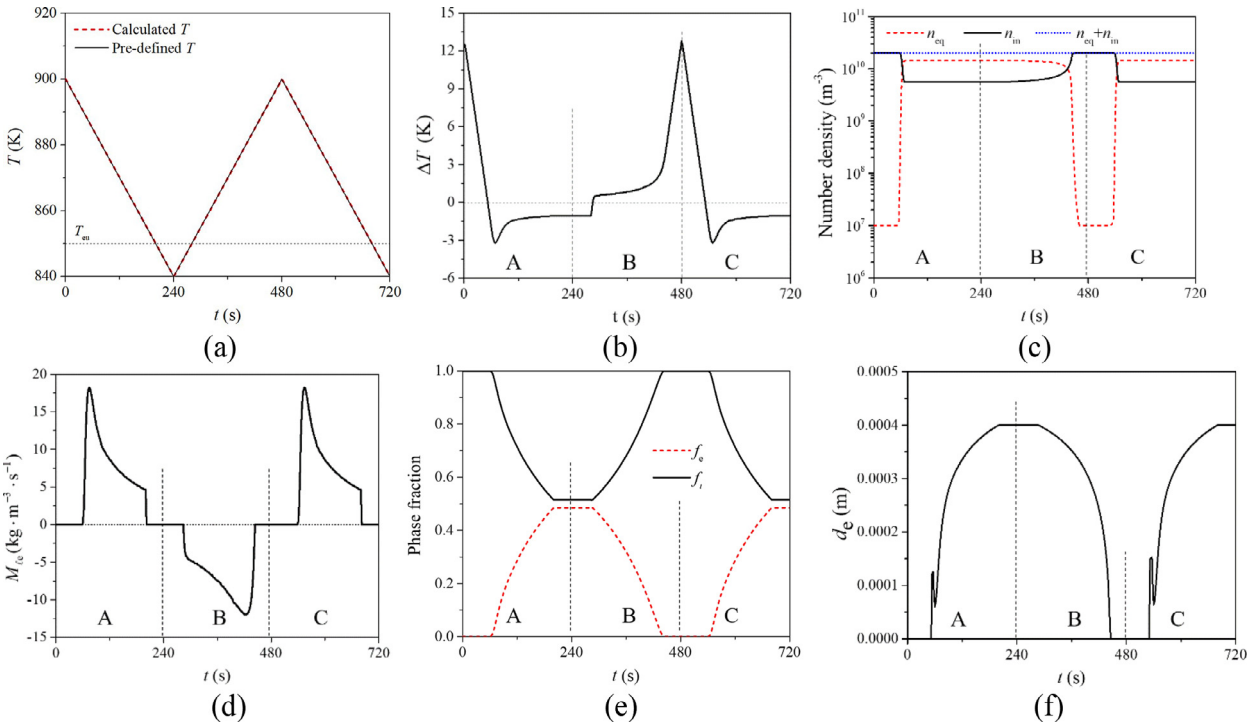

Fig. 3. Solidification/melting sequences of case I under purely diffusive conditions: (a) T; (b) ΔT; (c) n_{eq}, n_{in}, and the sum of n_{eq} and n_{in}; (d) $M_{\ell e}$; (e) f_ℓ and f_e; and (f) d_e.

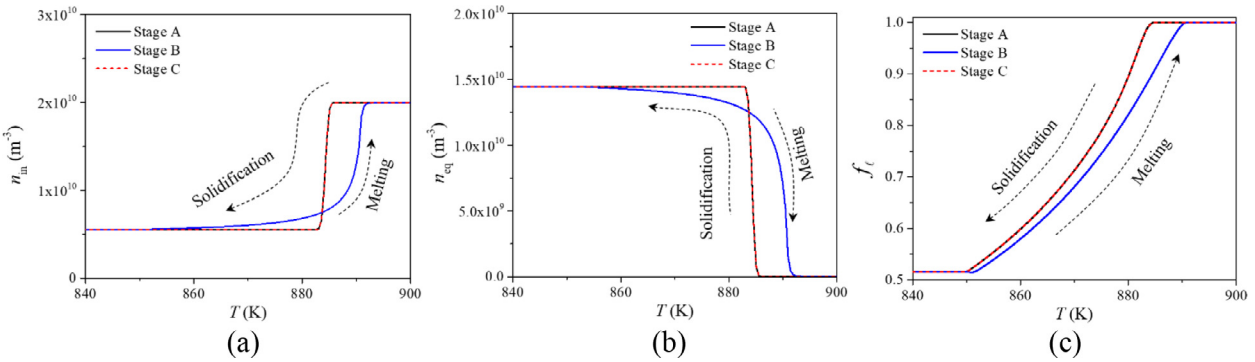

Fig. 4. Variations in (a) n_{in}, (b) n_{eq}, and (c) f_ℓ with T.

The melting sequence is shown in stage B in Fig. 3. T rose gradually, and ΔT changed from negative (undercooled) to positive (superheated). With the increase in T, the eutectic phase melted first, which was followed by melting of the equiaxed grains (as indicated by the negative $M_{\ell e}$). The equiaxed grains decreased in size (d_e) and phase fraction (f_e). At 420 s, when T rose to 884 K, n_{eq} decreased by 14.3% (from 1.4×10^{10} to 1.2×10^{10} m^{-3}), but d_e reduced by 40.0% (from 4.0×10^{-4} to 2.4×10^{-4} m) relative to the beginning of stage B. This is reasonable because a reduction in grain size (melting) always occurs before grain destruction. At 480 s, the minimum number density of grains was reached ($n_{eq} = 1.0 \times 10^{7}$ m^{-3}), and f_s and d_e vanished, indicating that all equiaxed grains had been melted and destroyed. In stage C (re-solidification), the sample was cooled again. The solidification in stage C repeated the results of stage A. As displayed in Fig. 3(c), the sum of n_{eq} and n_{in} was always conserved during the solidification and melting processes.

The variations in f_ℓ, n_{eq}, and n_{in} with T from stage A to C are plotted in Fig. 4. With decreasing T, the inoculants were activated as nuclei. With further solidification, f_ℓ decreased. In the opposite condition, when T rose, f_ℓ increased, and the equiaxed grains melted and finally turned into inoculants. The overlap of these lines is indicative of the excellent self-consistency of the current model and method.

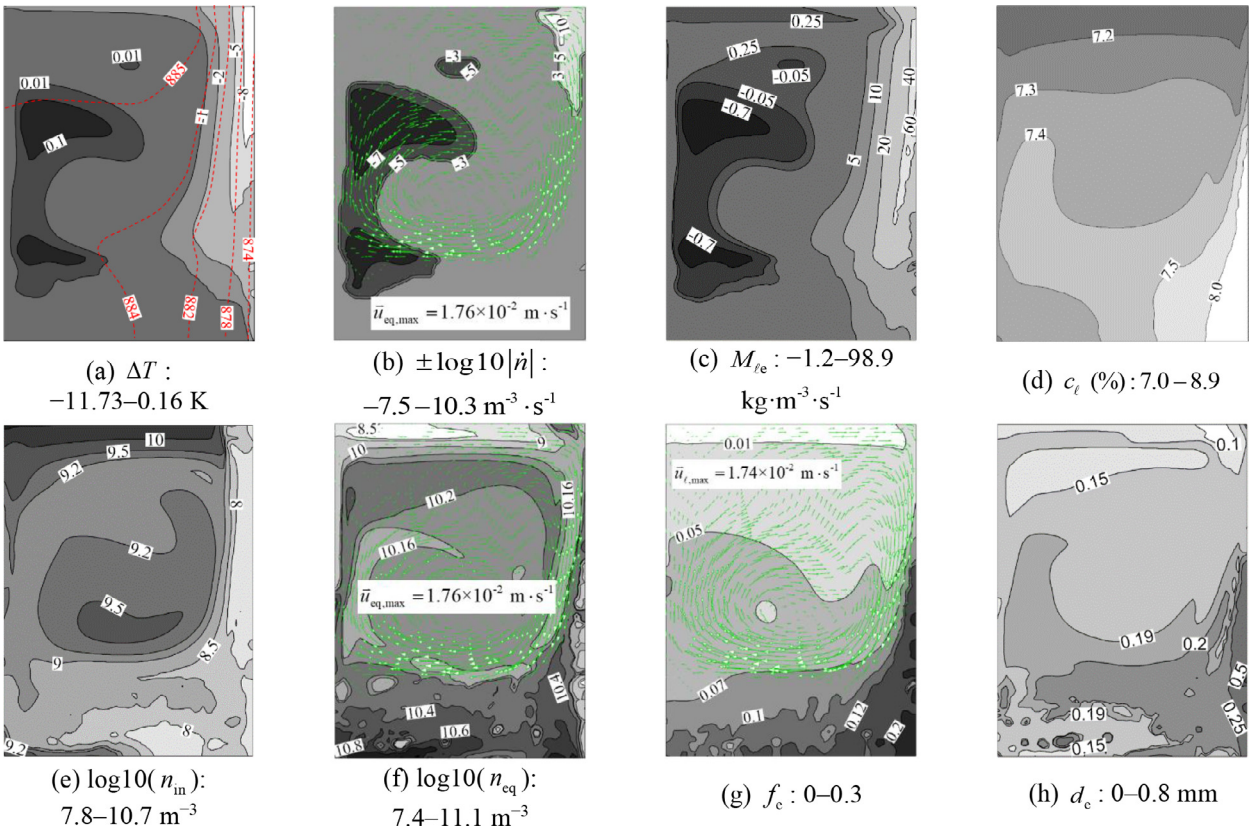

Fig. 5. Solidification sequence of case II (stage A) at 110 s. Contours and corresponding isolines of (a) ΔT overlaid by isotherms (red dashed lines); (b) $\pm\log10|\dot{n}|$ overlayed by the vectors of $\vec{u}_{eq}$; (c) $M_{\ell e}$; (d) c_ℓ; (e) log 10(n_{in}); (f) log 10(n_{eq}) overlaid by the vectors of $\vec{u}_{eq}$; (g) f_e overlaid by the vectors of $\vec{u}_\ell$; and (h) d_e (For interpretation of the references to color in this figure legend, the reader is referred to the web version of this article.).

4.2. Case II: solidification and melting under thermo-solutal convection

4.2.1. Case ii (stage A): cooling from the right side

Solidification was triggered by cooling from the right wall. The solidification sequence at 110 s is shown in Fig. 5. A clockwise thermo-solutal convection formed (Fig. 5(g)). The flow transported both the liquid and solid phases and modified the temperature field. T and ΔT are shown in Fig. 5(a), which shows that the melt was strongly undercooled near the right surface and slightly superheated in the left part. As shown in Fig. 5(b), in the upper-right corner where the melt was most undercooled ($\Delta T \approx -11$ K), the fastest nucleation rate was observed ($\dot{n} \approx 2.0\times10^{10} m^{-3}\cdot s^{-1}$). Because the grains were denser than the liquid, the formed grains sedimented and dragged the liquid melt to flow with them. Some of these newly formed equiaxed grains (with small size) were transported to the superheated region. As displayed in Fig. 5(c), the grains further solidified in the undercooled melt (as indicated by the positive $M_{\ell e}$), and those grains that were transported to the hot region melted ($M_{\ell e} < 0$). Re-melting accompanying solidification during casting process was numerically verified by the current model. As shown in Fig. 5(b), melting in the superheated region caused the grains to be destroyed, which reduced n_{eq} locally (as shown in Fig. 5(f)). Owing to solute partitioning ($m = 0.13$), solute-enriched liquid was rejected during the solidification process. High c_ℓ can be seen in Fig. 5(d) near the right surface. The rejected c_ℓ modified ΔT ($\Delta T = T_f + m\cdot c_\ell - T$) and thereby affected $M_{\ell e}$. n_{in} and n_{eq} are shown in Fig. 5(e)–(f), respectively. Nucleation consumed a large number of inoculants near the right surface (Fig. 5(b)), leading to a lower value of n_{in} in this region. After nucleation, the grains were transported along the vertical wall and piled up in the bottom ($n_{eq} \approx 10^{11}$ $m^{-3}\cdot s^{-1}$). The calculated f_e and d_e are shown in Fig. 5(g)–(h), respectively. The grains that nucleated on the surface adhered to the wall owing to the applied no-slip boundary condition. These grains grew quickly under strong undercooling, leading to a high f_e and large d_e on the right surface. In the lower-left corner, numerous small grains piled up. These small grains grew slowly because of the relatively high local temperature. From Fig. 5(g), it can be seen f_e was below f_e^c in the lower-left corner, which means that these small grains could be advected by liquid flow.

Analysis of the entire solidification sequence is shown in Fig. 6. During the early stage (0–120 s), the nucleation rate had a high magnitude of $\sim 10^{14} m^{-3}\cdot s^{-1}$ near the right wall (Fig. 6(a-1)–(a-2)). Afterwards, the formed grains sank and were transported by the flow (Fig. 6(b-1)–(b-2)). Most grains piled up in the bottom. The grains could grow further or be re-

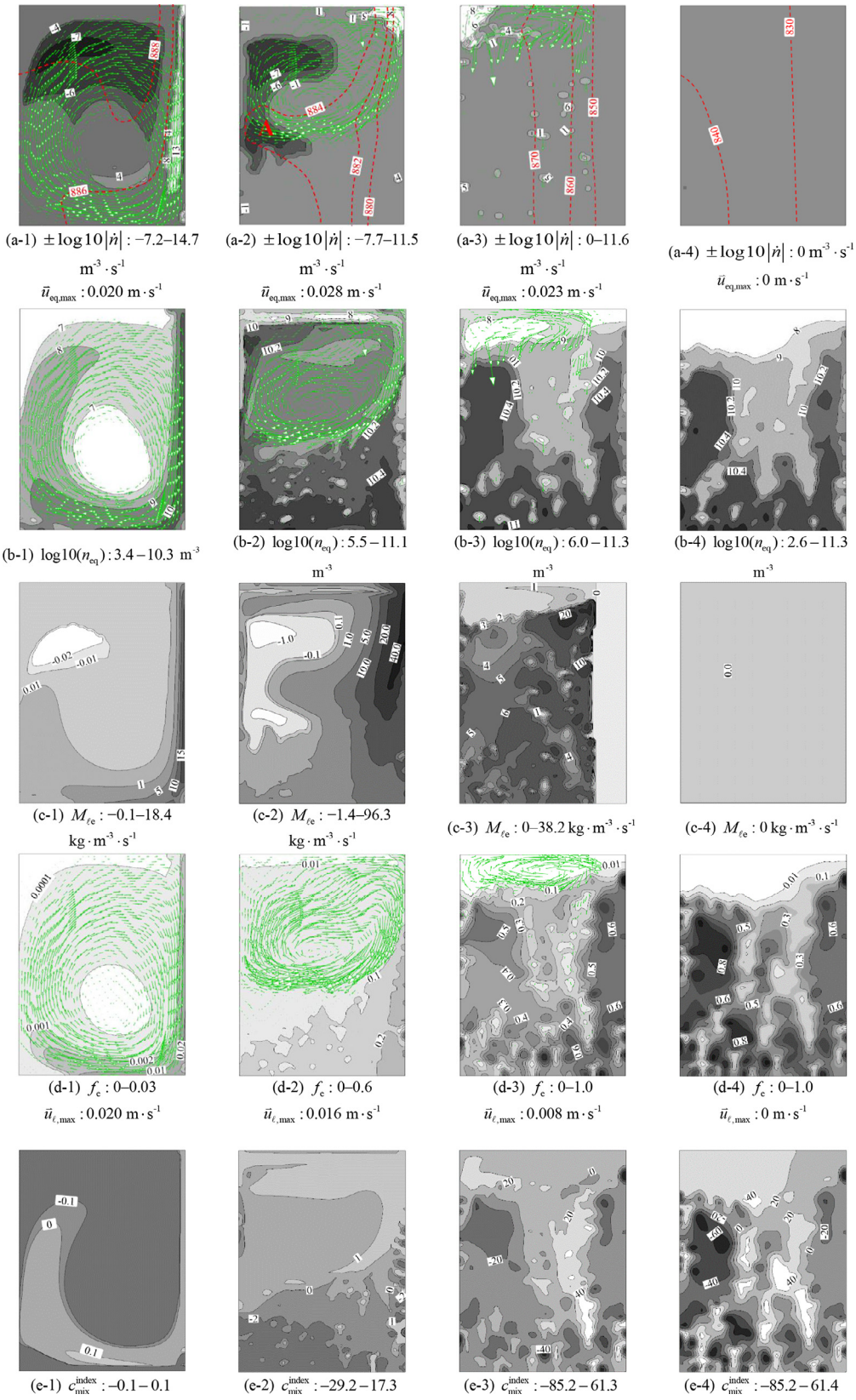

Fig. 6. Solidification sequence of case II (stage A). Contours and corresponding isolines of (a) $\pm\log10|\dot{n}|$ overlaid by the isolines of T (red dashed lines) and vectors of $\vec{u}_{eq}$; (b) $\log10(n_{eq})$ overlaid by the vectors of $\vec{u}_e$; (c) $M_{\ell e}$; (d) f_e overlaid by the vectors of $\vec{u}_\ell$; and (e) c_{mix}^{index}. Figures in the columns from left to right show the solidification sequence at 60, 120, 240, and 320 s, respectively. (For interpretation of the references to color in this figure legend, the reader is referred to the web version of this article.)

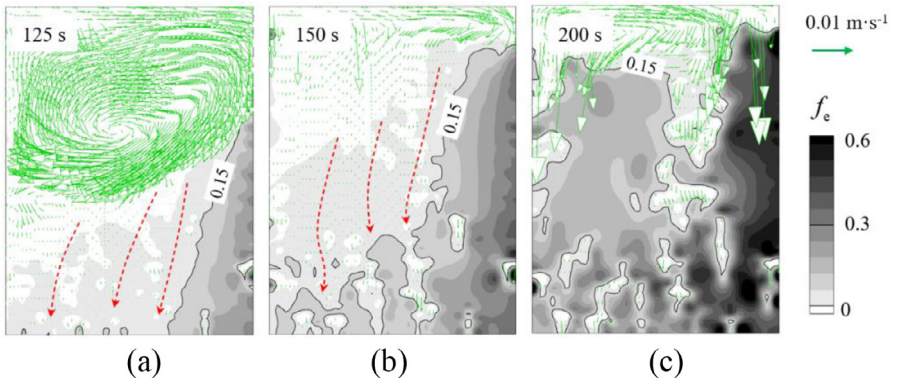

Fig. 7. Formation of a heterogeneous structure during solidification (case II, stage A). Contour of f_e overlaid by the vectors of $\vec{u}_{eq}$ (in green). The solid isoline denotes the grain packing front ($f_e = f_{si} \cdot f_e^c = 0.15$), and the red vectors indicate the grain sedimentation trajectory. (For interpretation of the references to color in this figure legend, the reader is referred to the web version of this article.)

melted/destroyed, depending on the local ΔT. As shown in Fig. 6(a-2) and (c-2), the grains continued to solidify ($M_{\ell e} > 0$) on the right side. On the left side, where the melt was relatively hot, the negative $M_{\ell e}$ indicates re-melting. The segregation index (c_{mix}^{index}) is shown in Fig. 6(e-1)–(e-2). The grains with a low solute concentration sank to the bottom, causing negative macrosegregation there. During the later stage (120–320 s), re-melting and grain destruction was almost impossible. As displayed in Fig. 6(d-3), only some liquid pockets survived in the lower part. Because of the small liquid regions, the liquid velocity was considerably smaller than the equiaxed velocity. As shown in Fig. 6(a-3), nucleation mainly occurred in the upper-left corner, where sufficient inoculants remained. In these liquid pockets, new grains were generated, but the nucleation rate was very low ($\dot{n} < 10^6 m^{-3} \cdot s^{-1}$). Fig. 6(b-3) depicts the distribution of n_{eq}. The grains were transported from the right to the left, and then sedimented there. Some small grains were advected to the liquid region, but most of the domain was almost completely solidified (Fig. 6(c-3)). When the temperature decreased to the eutectic temperature, the remaining liquid solidified as the eutectic phase. Fig. 6(d-3) and (e-3) present the distribution of f_e and c_{mix}^{index}, respectively. Negative macrosegregation can be observed in the region where f_e was large. The final solidification results are shown in Fig. 6(a-4)–(e-4). The volume average of n_{in} was equal to 3.7×10^8 m^{-3}, which indicates that most of the inoculants were activated as nuclei in the current case.

A value of 0.637 was used for the grain packing limit f_e^c. When $f_e > f_{si} \cdot f_e^c$, a rigid solid structure is generated. In Fig. 7, one solid isoline ($f_e = 0.15$) is drawn for the packing front. As shown in Fig. 7(a), in addition to the highly packed area in the lower-right corner, some lower-packed islands formed in the bottom. The equiaxed grains settled in the liquid–solid slurry. As presented in Fig. 7(b), the sedimentation and solidification of grains broadened the packed region, resulting in a heterogeneous solid structure. At a later moment (Fig. 7(c)), packed grains occupied most of the domain. Between the packed grains, there were some isolated liquid pockets, in which grains could still sink. Because the solid grains had a lower concentration than the surrounding eutectic phase, c_{mix}^{index} (Fig. 6(e)) exhibited a heterogeneous distribution similar to that of f_e (Fig. 6(d)).

4.2.2. Case ii (stage B): re-heating from the left side

The melting sequence at 380 s is presented in Fig. 8. The eutectic phase melted first at the eutectic isotherm, followed by gradual melting of the equiaxed grains. The left part of the domain was heated above the eutectic isotherm (Fig. 8(a)). After the eutectic phase melted, some liquid pockets were created, and a clockwise flow develops. The embedded grains (or grain clusters) were released and began to move again (Fig. 8(e)). c_ℓ (Fig. 8(b)) is large in region A, but it is relatively small in regions B and C. Because $\Delta T = T_f + m \cdot c_\ell - T$, ΔT is as a function of c_ℓ and T. As shown in Fig. 8(c), the alloy was overheated in region A and undercooled in regions B and C, which led to melting in region A and re-solidification in regions B and C (Fig. 8(d)). As shown in Fig. 8(e), from 320 to 380 s, d_e increased from 3.1 to 3.8 mm in region C and decreased from 0.48 to 0.37 mm in region A. The large grains sedimented quickly, but the small grains could easily be advected by the liquid flow. As shown in Fig. 8(f), nucleation occurred in regions B and C, but the nucleation rate was very small (~10^5 $m^{-3} \cdot s^{-1}$). In region A, the destruction rate was -7.1 $\times$ 10^7 $m^{-3} \cdot s^{-1}$. n_{eq} and n_{in} are presented in Fig. 8(g)–(h), respectively. Because only few grains were destroyed before this moment, there is no significant difference between Fig. 6 (b-4) and Fig. 8(g).

Analysis of the entire melting process is shown in Fig. 9. T and $M_{\ell e}$ are shown Fig. 9(a). In a majority of the domain, $M_{\ell e}$ was negative. In some regions (Fig. 9 (a-2)–(a-3)), $M_{\ell e}$ was positive, indicating local solidification. This can be better understood with the help of Fig. 8. The flow affects c_ℓ and T, and ΔT is calculated by $\Delta T = T_f + m \cdot c_\ell - T$. If c_ℓ is sufficiently high, the alloy can be undercooled even at an elevated T. Although local solidification was possible, the solidification rate was very small. Comparing Fig. 9(a)–(b), there was no new nucleation in the undercooled region. According to Fig. 9 (b-3), the maximum destruction rate during the late stage of the melting process (615 s) was $-$ 3.2 $\times$ 10^{10} $m^{-3} \cdot s^{-1}$, which is

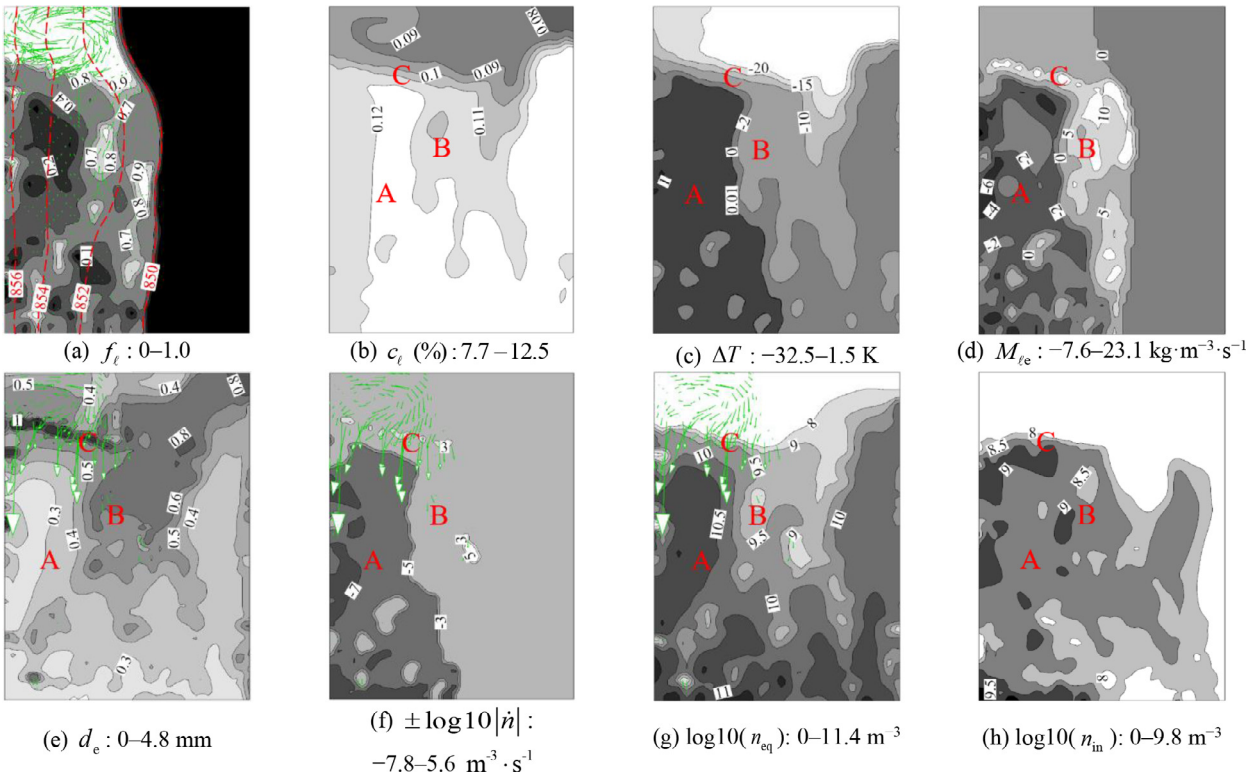

Fig. 8. Melting sequence of case II (stage B) at 380 s. Contours and corresponding isolines of (a) f_ℓ overlaid by the isotherms (red dashed lines) and vectors of $\vec{u}_\ell$; (b) c_ℓ; (c) ΔT; (d) $M_{\ell e}$; (e) d_e overlaid by the vectors of $\vec{u}_{eq}$; (f) $\pm\log10|\dot{n}|$ overlaid by the vectors of $\vec{u}_e$; (g) log 10(n_{eq}) overlaid by the vectors of $\vec{u}_{eq}$; and (h) log10(n_{in}). (For interpretation of the references to color in this figure legend, the reader is referred to the web version of this article.)

three orders of magnitude larger than that at 380 s (Fig. 8(f)). f_e and n_{eq} are shown in Fig. 9(c)–(d), respectively. As melting progressed, f_e decreased, and when $f_e < f_{si}\cdot f_e^c$, the grains were movable. As the liquid regions expanded, the liquid velocity became increasingly stronger. Equiaxed grains were transported to the superheated regions and be melted/destroyed. The evolution of c_{mix}^{index} is shown in Fig. 9(e). As melting progressed, fresh liquid with a low solute concentration was released, which diluted the positive segregation. From 500 to 640 s, c_{mix}^{index} at point A was reduced from 32.6 to 3.2.

An interesting phenomenon was observed: transport of a bulk grain network during melting, as shown in Fig. 10. Two isolines are drawn: $f_e = 0.01$ (indicating the melt front), and $f_e = 0.15$ (indicating the packing front). At 600 s (Fig. 10(a)), more than half of the domain had melted. The packed region is marked as A, B, and C. Region A is connected to the main solid part (region C) through a thin bridge (region B). Two flow vortices developed, which were separated by the rigid solid structure. Only the liquid could flow through this rigid porous medium. At 610 s (Fig. 10(b)), region B had re-melted. Region A detached from region C, but it was still partially connected to the left wall. At 615 s (Fig. 10(c)), region A detached from the left wall and turned into the bulk melt region. The red vectors in Fig. 10 indicate the direction of rotation. In the subsequent melting process, this bulk grain network became increasingly smaller until it was completely melted.

5. Discussion

This work is an extension of the previous volume-average solidification model [4,22,24,26], which considers melting and grain destruction. Because this extension is implemented based on an ideal scenario of two-phase globular equiaxed solidification, for which no direct experiments are available to compare, numerical parameter studies were performed (1) to demonstrate the importance of melting and grain destruction during alloy solidification and (2) to investigate the effect of uncertainty in the parameters.

5.1. Importance of melting/grain destruction

To illustrate the importance of melting during solidification, an extra simulation case was conducted. All the settings were the same as those in case II (stage A) except that melting was ignored. A comparison between the simulation results of the two cases at 120 s is shown in Fig. 11. As shown in Fig. 11(a), melting occurred near the left wall region.

Re-melting consumed some latent heat, leading to a decrease in the local temperature. In comparison with the case without melting (Fig. 11(b)), the case with melting (Fig. 11(a)) predicted a slightly lower local temperature near the left wall. In Fig. 11(c), the contour of the sum of the re-melted mass, $\int_0^t M_{\ell e} dt$, during the entire cooling (solidification) process is shown. Equiaxed grains, which were transported from other regions to the left wall region, re-melted. The volume average of $\iiint_{vol} (\int_0^t M_{\ell e} dt) dV$ inside the solid isoline in Fig. 11(c) was -8.3 kg·m^{-3}. Re-melting 8.3 kg·m^{-3} of equiaxed grains will dilute the local melt concentration there. Correspondingly, 3.3×10^6 J · m^{-3} of energy will be consumed as the latent heat of melting. The re-melting of the as-formed solid phase is an important mechanism of species and energy transport.

In the solidification model, if the accompanying melting and grain destruction were ignored, the volume integral of n_{eq} in the entire sample domain of the as-solidified sample would be overestimated by ~2.0%, the volume integral of f_e would be overestimated by ~1.7%, the volume integral of d_e would be underestimated by ~3.0 μm, and the integral of $|c_{mix}^{index}|$ would be underestimated by ~0.9. Note that the casting sample used in the current study was very small, and

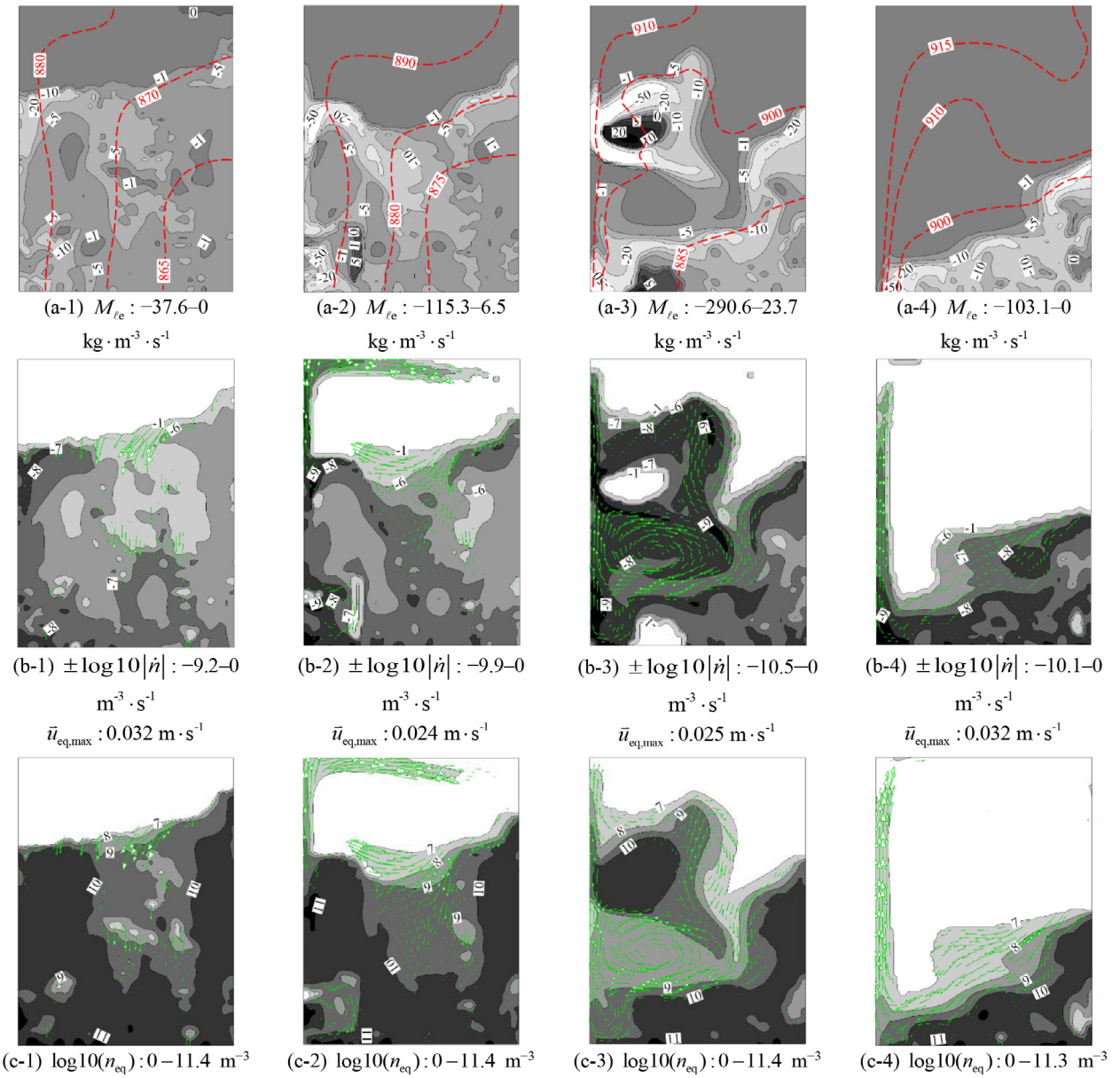

Fig. 9. Melting sequence of case II (stage B). Contours and corresponding isolines of (a) $M_{\ell e}$ overlaid by T (red dashed lines); (b) $\pm\log10|\dot{n}|$ overlaid by the vectors of $\vec{u}_{eq}$; (c) $\log10(n_{eq})$ overlaid by the vectors of $\vec{u}_{eq}$; (d) f_e overlaid by the vectors of $\vec{u}_{\ell}$; and (e) c_{mix}^{index}. Figures in the columns from left to right show the melting sequences at 500, 560, 615, and 640 s, respectively. (For interpretation of the references to color in this figure legend, the reader is referred to the web version of this article.)

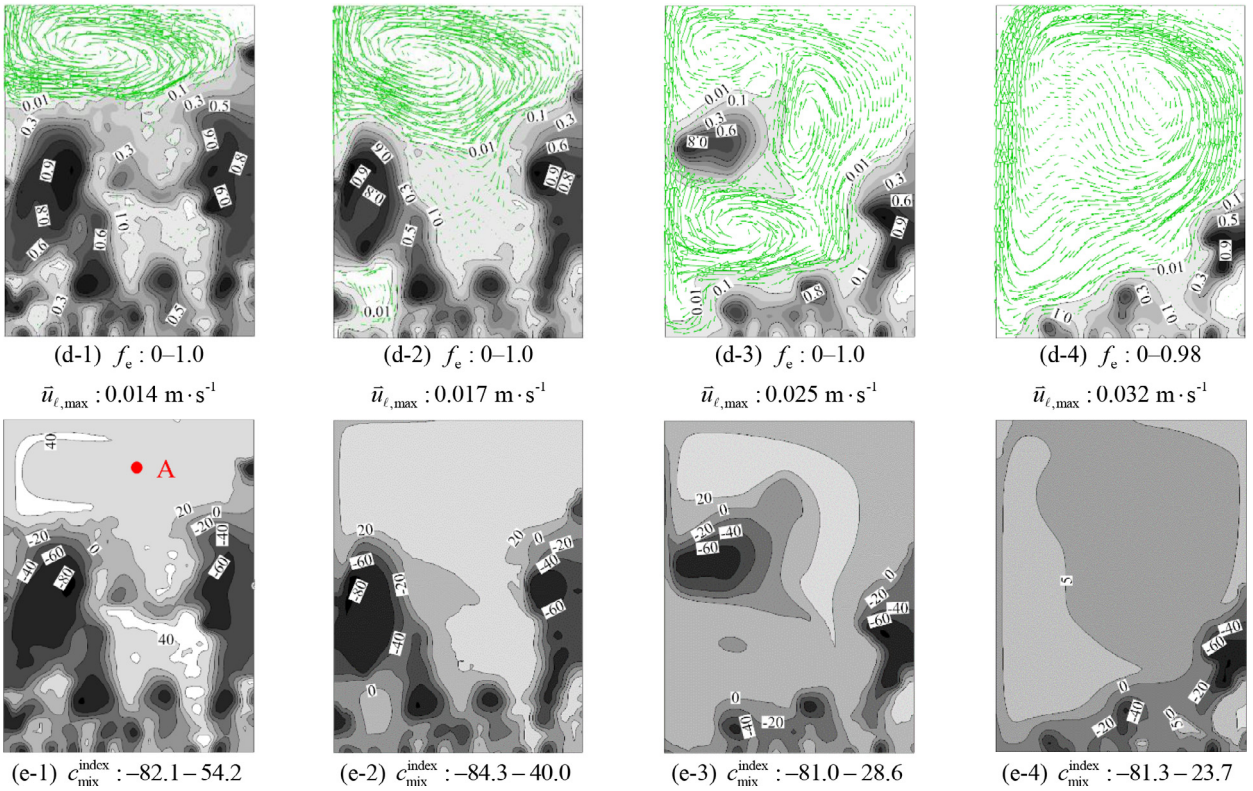

Fig. 9. Continued

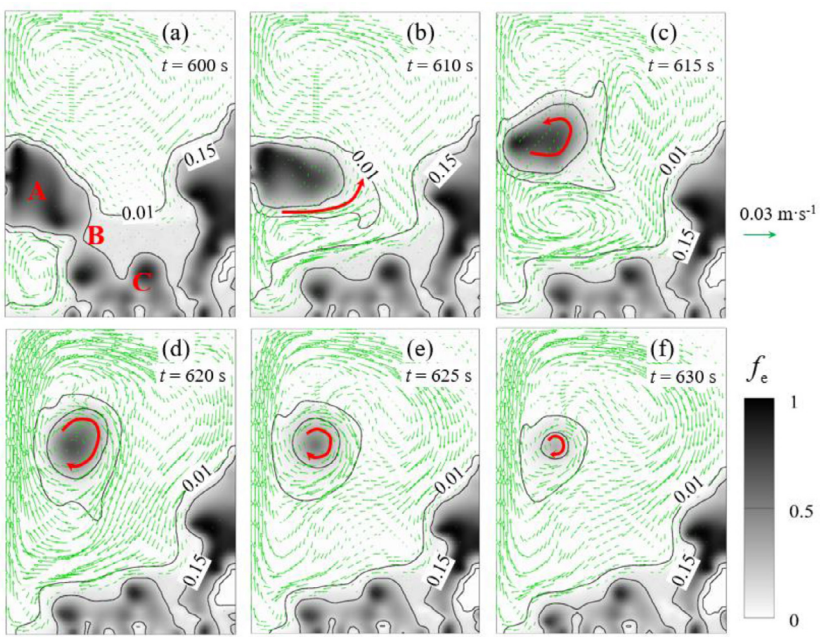

Fig. 10. Transport of a bulk grain network during the melting process shown by the contours of f_e overlaid by the vectors of $\vec{u}_\ell$. The red vectors indicate the rotation direction of the bulk grain network. (For interpretation of the references to color in this figure legend, the reader is referred to the web version of this article.)

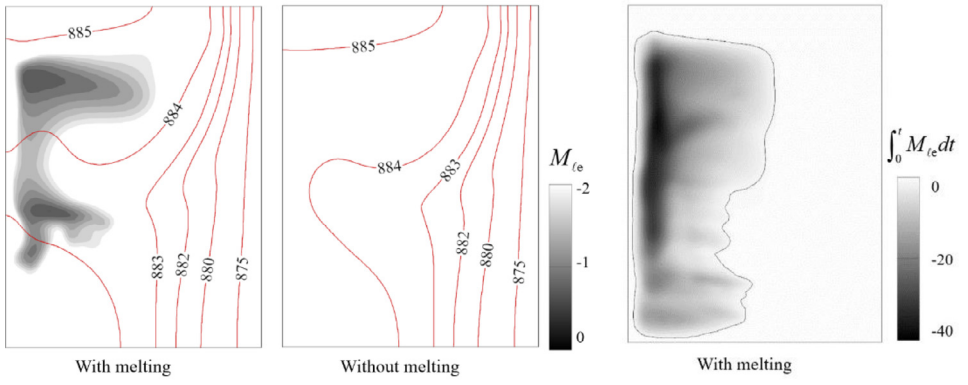

Fig. 11. Comparison of two simulations for case II (stage A): (a) with melting and (b) without melting at 120 s. In (a), the contour of $M_{\ell e}$ (only $M_{\ell e} < 0$ is shown) is overlaid by isotherms. (c) Contour of the sum of the re-melted mass $\int_0^t M_{\ell e} dt$ during the entire cooling (solidification) process.

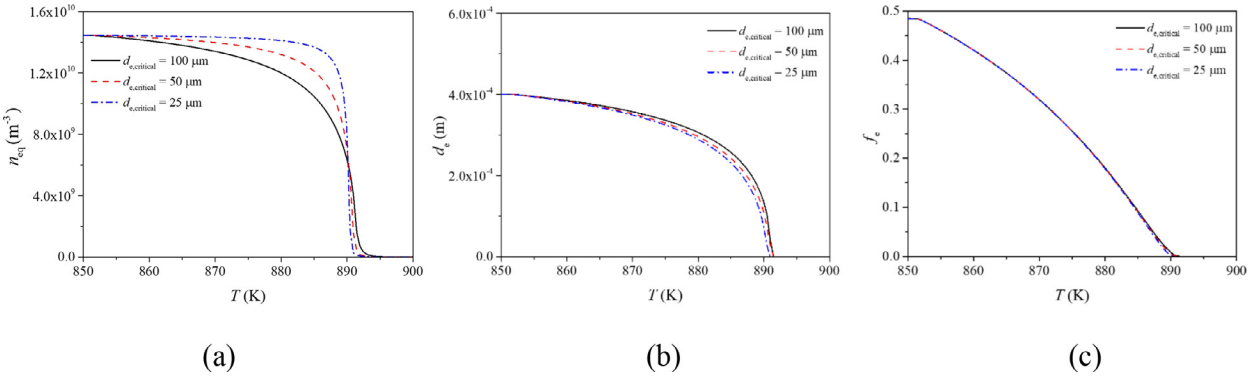

Fig. 12. Effect of $d_{e,critical}$ on the calculated (a) n_{eq}, (b) d_e, and (c) f_e as a function of T. These simulations were performed based on case I (stage B), and all quantities were taken from the domain centre.

the aforementioned differences were not very significant. However, the role of re-melting and grain destruction, which accompany alloy solidification, would become more obvious for casting with larger dimensions. For example, in engineering ingot or continuous castings, the melt flow and grain transport are approximately 1–2 orders of magnitude more intensive. Therefore, the re-melting effect should be more significant.

5.2. Effect of $d_{e,critical}$

$d_{e,critical}$ was introduced as the critical grain size for grain destruction. Determining the exact value of $d_{e,critical}$ is beyond the scope of this study. However, a numerical parameter study can be performed to analyse the sensitivity of the melting process to its value. The calculated n_{eq}, d_e, and f_e are shown in Fig. 12(a)–(c), respectively. As expected, when $d_{e,critical}$ was larger, n_{eq} decreased faster, and d_e became larger. However, $d_{e,critical}$ has a minimal effect on f_e. This is understandable because n_{eq} and f_e are calculated from their conservation equations, out of which the volume-averaged grain size is derived: $d_e = \sqrt[3]{6 f_e / \pi n_{eq}}$. The combination of decreased n_{eq} and increased d_e results in almost no change in the solidification; hence, f_e appears to be independent from $d_{e,critical}$. It should be stressed that $d_{e,critical}$ cannot be too small or too large. Physically, $d_{e,critical}$ should be larger than the size of inoculants (~2 μm). An excessive $d_{e,critical}$ results in equiaxed grains that cannot be realistically melted in one time step ($\Delta t = 0.001$s). From the parameter study shown in Fig. 12, the calculated d_e and f_e appear to not be sensitive to the chosen $d_{e,critical}$ when its value falls in the range 25–100 μm, but the exact value of $d_{e,critical}$ requires further investigation.

5.3. Mesh sensitivity study

Simulations with three different mesh sizes ($\Delta x = 2.0$, 1.0, and 0.5 mm) were performed to examine the mesh sensitivity. The distribution of f_e in the as-solidified sample is shown in Fig. 13. Although the distributions of f_e were not identical,

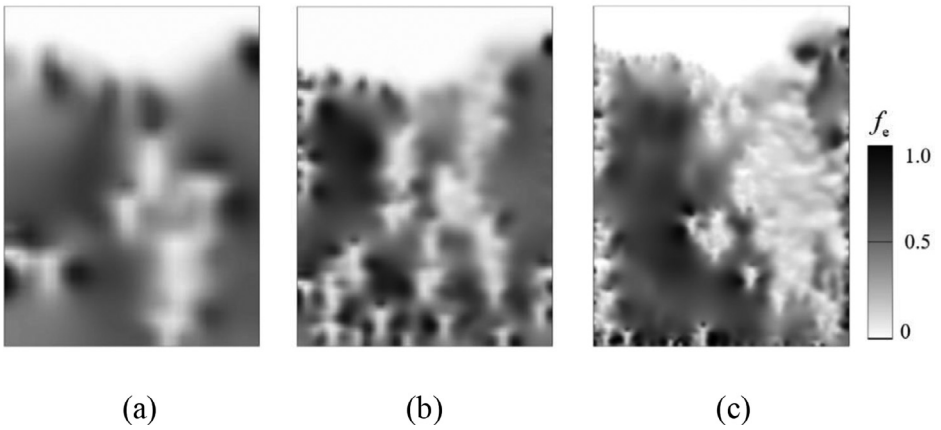

Fig. 13. Simulation results with different mesh size: (a) Δx = 2.0mm, (b) Δx = 1.0mm, and (c) Δx = 0.5mm. The contour denotes f_e at the end of solidification. These simulations were performed based on case II (stage A).

an equiaxed-free region was observed in the upper-left corner of all simulations. For all three simulations, the volume-averaged f_e over the entire casting domain was 41.6, 39.7, and 38.3%, and the volume-averaged $|c_{mix}^{index}|$ was 21.9, 25.1, and 25.0, respectively. With the current mesh size, it is not possible to get a quantitatively converged result. However, it can be safely concluded that calculations with a mesh size smaller than 1.0 mm can reproduce the phase distribution pattern.

5.4. Grain packing

f_e^c plays important role in the formation of the as-solidified microstructure and macrosegregation. Some previous models used a value of 0.637 for f_e^c by assuming ideal face-centred close packing of equal-diameter spheres [4,22,29,43,44], while most industry alloys with dendritic solidification would pack at a much lower f_e^c, e.g. 0.27 was used for an Al–22 wt.% Cu alloy [39] and 0.4 for a steel ingot [45]. Most recent works have shown that as the morphology of the particles changes from spherical towards a more nonconvex geometry, the packing fraction decreases [46,47]. Plotkowski and Krane [48,49] investigated the effect of the local velocity field on the likelihood of packing. They proposed that particles were more likely to pack if their velocity was directed towards a packed interface, and less likely to attach when they were advected away from the interface. Experimental data for different alloys revealed that the packing limit could be reached when the solid fraction was approximately 0.1–0.3 in large-grained casting [24,50,51].

Similar to previous studies [4,22,29,43,44], f_e^c was assumed to equal to 0.637 in this study. As aforementioned, a simplified dendritic morphology of equiaxed grain was considered to calculate the hydrodynamic interactions. When the solid grain is considered as an equiaxed grain envelope, the corresponding packing solid fraction can be evaluated by $f_e = f_e^c \cdot f_{si}$. In this study, because f_e^c =0.637 and f_{si}=0.235, the corresponding packing solid fraction is equal to 0.15. f_{si} is a parameter related to the morphology of the equiaxed grain. A numerical study was performed to study the effect of f_{si} on the solidification results. The simulation results at 100 s for three different f_{si} are compared in Fig. 14(a). When a small f_{si} was used (dendritic grain), the grains packed shortly after nucleation. When a large f_{si} was used (globular grain), more grains could be transported, causing grains to pile up at the bottom. The as-solidified structure is shown in Fig. 14(b). A large f_{si} was beneficial for phase separation and therefore the extension of the equiaxed-free (pure eutectic) region at the top.

In the current paper, two cases were designed to study the melting and grain destruction phenomena during equiaxed solidification. The first simple case (Case I) is a 0-dimensional case, i.e. the simulation results represent the solidification/melting in one isolated volume element. No flow and grain transport are considered. With this simple case, one can verify all modelling concepts/assumptions in mathematical way. The second case (Case II) is closer to reality, but not consistent with a real casting. Flow and grain transport in 2-dimensional situation are considered, but still some assumptions were made and some modelling parameters might not be realistic. For example, a real casting mostly solidifies in a mixed columnar-equiaxed solidification. Here, the columnar structure has to be ignored in this step. Nevertheless, this modelling step (Case II) is very necessary. It helps to verify the modelling capacity (functionalities) for the remelting/grain destruction with melt flow and grain transport. Although the modelling result is difficult to compare with that of a real casting benchmark quantitatively, the modelling result can qualitatively explore important phenomena which would occur in real castings. The next step of the modelling part would be to compare quantitatively with real casting benchmark. For that purpose, some unrealistic assumptions (e.g. ignorance of columnar structure) must be released, and reliable modelling parameters must be determined through parameter studies and necessary experimental measurements. This work will continue, especially regrading to validation of the model by comparison with more realistic benchmark and laboratory casting experiments.

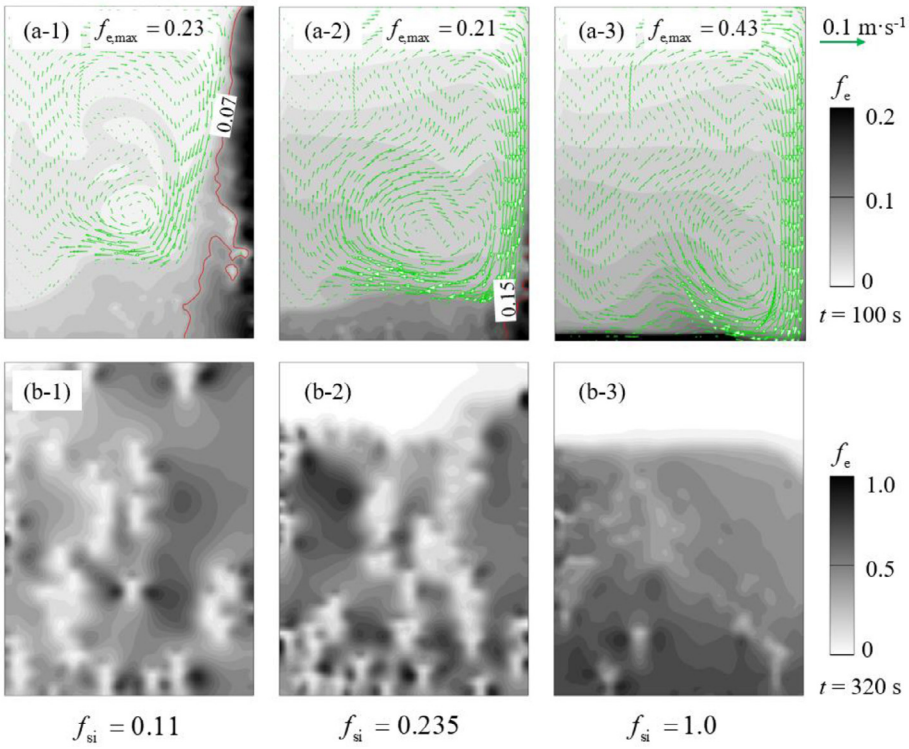

Fig. 14. Effect of f_{si} (0.11, 0.235, and 1.0) on the simulation results. (a-1)–(a-3) Simulation results at 100 s with the contours of f_e overlaid by the vectors of $\vec{u}_{eq}$. The red isolines of $f_e = f_e^c \cdot f_{si}$ in (a-1) and (a-2) indicate the packing fronts. (b-1)–(b-3) Simulation results with the contours of f_e at the end of solidification. These simulations were performed based on case II (stage A). (For interpretation of the references to color in this figure legend, the reader is referred to the web version of this article.)

6. Conclusions

A volume-average-based two-phase globular equiaxed solidification model was extended to include the melting and grain destruction. To verify the model, simulations of solidification/melting of a 2D rectangular Al–7 wt.% Si casting were performed.

Under the purely diffusive solidification/melting condition, the sum of the number densities of the inoculants (free growth sites) and activated equiaxed grains ($n_{in} + n_{eq}$) was always locally conserved. Although the same diffusion-governed kinetics applied for growth and size-reduction of the equiaxed grains, the obtained $f_\ell - T$ curves during cooling (solidification) and heating (melting) were not identical. Therefore, melting cannot be simply considered to be inverse solidification.

With the addition of thermo-solutal convection and grain transport, it is only the volume integral of the number densities of the inoculants and activated equiaxed grains over the entire casting domain ($\Sigma(n_{in} + n_{eq})$) that is conserved. During cooling (solidification), some as-nucleated equiaxed grains were transported to superheated regions where re-melting and grain destruction occurred. In the opposite condition, during heating (melting), there were some locally undercooled regions where nucleation and solidification could occur. This simultaneous solidification/melting phenomenon presents an important species/energy transport mechanism, influencing the structural and compositional heterogeneity of the final as-cast product.

Acknowledgments

The authors acknowledge the financial support from Austrian Research Promotion Agency (FFG) -Austrian Space Application Program (ASAP) through the project FLOWSICONS (No. 859777), Austria Science Fund (FWF, I4278-N36), as well as the support from European Space Agency (ESA) through the project MICAST.

Appendix A. Lognormal grain size distribution

The lognormal distribution is widely used in the probabilistic description of engineering quantities that only have positive values [52–55]. It is introduced here to characterise the grain size distribution. The probability distribution function (PDF)

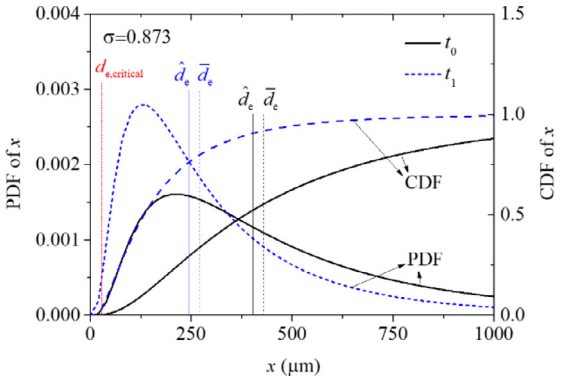

Fig. A1. Description of the melting process (from t_0 to t_1) with a lognormal grain size distribution. PDF: probability distribution function; CDF: cumulative distribution function.

of grain size is written as

$$f(x) = \frac{1}{\sqrt{2\pi}\sigma x} e^{-\frac{1}{2}\left(\frac{\ln(x)-\ln(\hat{d}_e)}{\sigma}\right)^2}, \tag{A.1}$$

where x is the dummy variable corresponding to the grain diameter of different size classes, σ is the geometric standard deviation, and $\hat{d}_e$ is the geometric mean of the grains:

$$\hat{d}_e = \sqrt[n]{\prod_{i=1}^{n} d_{e,i}}. \tag{A.2}$$

The PDF and the corresponding cumulative distribution function (CDF) of the grain size at two different moments (t_0 and t_1) are shown in Fig. A1. As melting occurs between t_0 and t_1, $\hat{d}_e$ decreases, and the PDF curve changes correspondingly. Note that the volume-averaged grain diameter d_e is calculated by

$$d_e = \sqrt[3]{\frac{6f_e}{\pi n_{eq}}}, \tag{A.3}$$

which is not equal to $\hat{d}_e$. For the current volume-average model, only a volume-averaged grain diameter can be obtained. In this paper, $\hat{d}_e$ is approximated by d_e. A further assumption is made: the variation in d_e and $\hat{d}_e$ due to melting follows the same trend, i.e. $d(\hat{d}_e)/dt \approx d(d_e)/dt$, which can be estimated by v_{Re}.

References

[1] D.J. Allen, J.D. Hunt, Melting during solidification, Metall. Trans. A. 7 (1976) 767–770, doi:10.1007/BF03186812.
[2] M. Rettenmayr, Melting and remelting phenomena, Int. Mater. Rev. 54 (2009) 1–17, doi:10.1179/174328009X392930.
[3] M.E. Glicksman, Melting kinetics in microgravity, J. Phys. Conf. Ser. 327 (2011) 012001, doi:10.1088/1742-6596/327/1/012001.
[4] J. Ni, C. Beckermann, Modeling of globulitic alloy solidification with convection, J. Mater. Process. Manuf. Sci. 2 (1993) 217–231.
[5] J.W. Gao, C.Y. Wang, An experimental investigation into the effects of grain transport on columnar to equiaxed transition during dendritic alloy solidification, J. Heat Transf. 121 (1999) 430–437, doi:10.1115/1.2825996.
[6] J.W. Gao, C.Y. Wang, Effects of grain transport on columnar to equiaxed transition in dendritic alloy solidification, Model. Cast. Weld. Adv. Solidif. Process. VIII (1998) 425–432.
[7] W. Kurz, D.J. Fisher, R. Trivedi, Progress in modelling solidification microstructures in metals and alloys: dendrites and cells from 1700 to 2000, Int. Mater. Rev. 64 (2019) 311–354, doi:10.1080/09506608.2018.1537090.
[8] W.J. Boettinger, S.R. Coriell, A.L. Greer, A. Karma, W. Kurz, M. Rappaz, R. Trivedi, Solidification microstructures: recent developments, future directions, Acta Mater. 48 (2000) 43–70, doi:10.1016/S1359-6454(99)00287-6.
[9] C. Beckermann, R. Viskanta, M. Buchmann, M. Rettenmayr, Microstructure evolution during melting and resolidification in a temperature gradient, J. Cryst. Growth 284 (2005) 544–553, doi:10.1016/j.jcrysgro.2005.06.044.
[10] L.S. Yao, J. Prusa, Melting and Freezing, Adv. Heat Transf. 19 (1989) 1–95, doi:10.1016/S0065-2717(08)70211-9.
[11] A. Kumar, P. Dutta, S. Sundarraj, M.J. Walker, Remelting of solid and its effect on macrosegregation during solidification, Numer. Heat Transf. Part A Appl. 51 (2007) 59–83, doi:10.1080/10407780600710391.
[12] U. Bösenberg, M. Buchmann, M. Rettenmayr, Initial transients during solid/liquid phase transformations in a temperature gradient, J. Cryst. Growth 304 (2007) 281–286, doi:10.1016/j.jcrysgro.2007.03.001.
[13] C. Gau, R. Viskanta, Melting and solidification of a pure metal on a vertical wall, J. Heat Transfer. 108 (1986) 174–181, doi:10.1115/1.3246884.
[14] Y. Wang, A. Amiri, K. Vafai, An experimental investigation of the melting process in a rectangular enclosure, Int. J. Heat Mass Transf. 42 (1999) 3659–3672, doi:10.1016/S0017-9310(99)00024-1.
[15] H. Yin, J.N. Koster, Double-diffusive convective flow and interface morphology during transient Ga-5% In alloy melting, J. Cryst. Growth 217 (2000) 170–182, doi:10.1016/S0022-0248(00)00411-5.
[16] R.S. Rerko, H.C. de Groh, C. Beckermann, Effect of melt convection and solid transport on macrosegregation and grain structure in equiaxed Al-Cu alloys, Mater. Sci. Eng. A 347 (2003) 186–197, doi:10.1016/S0921-5093(02)00592-0.
[17] H. Hu, S.A. Argyropoulos, Mathematical modelling of solidification and melting: a review, Model. Simul. Mater. Sci. Eng. 4 (1996) 371–396, doi:10.1088/0965-0393/4/4/004.

[18] S. Jana, S. Ray, F. Durst, A numerical method to compute solidification and melting processes, Appl. Math. Model. 31 (2007) 93–119, doi:10.1016/j.apm.2005.08.012.
[19] H. Zhang, M. Charmchi, D. Veilleux, M. Faghri, Numerical and experimental investigation of melting in the presence of a magnetic field: simulation of low-gravity environment, J. Heat Transfer. 129 (2007) 568–576, doi:10.1115/1.2709961.
[20] V.R. Voller, A. Mouchmov, M. Cross, An explicit scheme for coupling temperature and concentration fields in solidification models, Appl. Math. Model. 28 (2004) 79–94, doi:10.1016/S0307-904X(03)00115-X.
[21] Q. Zhang, H. Fang, H. Xue, Q. Tang, S. Pan, M. Rettenmayr, M. Zhu, Modeling of melting and resolidification of equiaxed microstructures in a temperature gradient, Scr. Mater. 151 (2018) 28–32, doi:10.1016/j.scriptamat.2018.03.031.
[22] M. Wu, A. Ludwig, A. Bührig-Polaczek, M. Fehlbier, P.R. Sahm, Influence of convection and grain movement on globular equiaxed solidification, Int. J. Heat Mass Transf. 46 (2003) 2819–2832, doi:10.1016/S0017-9310(03)00054-1.
[23] M. Wu, A. Ludwig, Modeling equiaxed solidification with melt convection and grain sedimentation-I: model description, Acta Mater 57 (2009) 5621–5631, doi:10.1016/j.actamat.2009.07.056.
[24] C.Y. Wang, C. Beckermann, Equiaxed dendritic solidification with convection: part I. Multiscale/multiphase modeling, Metall. Mater. Trans. A Phys. Metall. Mater. Sci. 27 (1996) 2754–2764, doi:10.1007/BF02652369.
[25] J. Ni, C. Beckermann, A volume-averaged two-phase model for transport phenomena during solidification, Metall. Trans. B. 22 (1991) 349–361, doi:10.1007/BF02651234.
[26] A. Ludwig, M. Wu, Modeling of globular equiaxed solidification with a two-phase approach, Metall. Mater. Trans. A Phys. Metall. Mater. Sci. 33 (2002) 3673–3683, doi:10.1007/s11661-002-0241-z.
[27] J.P. Gu, C. Beckermann, A.F. Giamei, Motion and remelting of dendrite fragments during directional solidification of a nickel-base superalloy, Metall. Mater. Trans. A Phys. Metall. Mater. Sci. 28 (1997) 1533–1542, doi:10.1007/s11661-997-0215-2.
[28] Y. Zheng, M. Wu, A. Kharicha, A. Ludwig, Numerical analysis of macrosegregation in vertically solidified Pb-Sn test castings-part II: equiaxed solidification, Comput. Mater. Sci. 124 (2016) 456–470, doi:10.1016/j.commatsci.2016.07.018.
[29] M. Wu, A. Ludwig, A. Kharicha, Volume-averaged modeling of multiphase flow phenomena during alloy solidification, Metals 9 (2019) 229 Basel, doi:10.3390/met9020229.
[30] R.B. Bird, W.E. Stewart, E.N. Lightfoot, Transport Phenomena, Revised 2n, 2006. 10.1002/aic.690070245.
[31] A.L. Greer, P.S. Cooper, M.W. Meredith, W. Schneider, P. Schumacher, J.A. Spittle, A. Tronche, Grain refinement of aluminium alloys by inoculation, Adv. Eng. Mater. 5 (2003) 81–91, doi:10.1002/adem.200390013.
[32] A.M. Bunn, P. Schumacher, M.A. Kearns, C.B. Boothroyd, A.L. Greer, Grain refinement by Al-Ti-B alloys in aluminium melts: a study of the mechanisms of poisoning by zirconium, Mater. Sci. Technol. 15 (1999) 1115–1123, doi:10.1179/026708399101505158.
[33] M. Rappaz, Modelling of microstructure formation in solidification processes, Int. Mater. Rev. 34 (1989) 93–124, doi:10.1179/imr.1989.34.1.93.
[34] M. Rappaz, C.A. Gandin, Probabilistic modelling of microstructure formation in solidification processes, Acta Metall. Mater. 41 (1993) 345–360, doi:10.1016/0956-7151(93)90065-Z.
[35] M. Wu, A. Ludwig, Using a three-phase deterministic model for the columnar-to-equiaxed transition, Metall. Mater. Trans. A Phys. Metall. Mater. Sci. 38 A (2007) 1465–1475, doi:10.1007/s11661-007-9175-9.
[36] C.A. Gandin, M. Rappaz, A coupled finite element-cellular automaton model for the prediction of dendritic grain structures in solidification processes, Acta Metall. Mater. 42 (1994) 2233–2246, doi:10.1016/0956-7151(94)90302-6.
[37] T.E. Quested, A.L. Greer, Grain refinement of Al alloys: mechanisms determining as-cast grain size in directional solidification, Acta Mater. 53 (2005) 4643–4653, doi:10.1016/j.actamat.2005.06.018.
[38] Y. Zheng, M. Wu, E. Karimi-Sibaki, A. Kharicha, A. Ludwig, Use of a mixed columnar-equiaxed solidification model to analyse the formation of as-cast structure and macrosegregation in a Sn-10 wt% Pb benchmark experiment, Int. J. Heat Mass Transf. 122 (2018) 939–953, doi:10.1016/j.ijheatmasstransfer.2018.02.012.
[39] M. Bedel, K.O. Tveito, M. Založnik, H. Combeau, M. M'Hamdi, A model study of the impact of the transport of inoculant particles on microstructure formation during solidification, Comput. Mater. Sci. 102 (2015) 95–109, doi:10.1016/j.commatsci.2015.01.028.
[40] H. Zhang, M. Wu, S.N. Tewari, A. Ludwig, A. Kharicha, Geometrical effect on macrosegregation formation during unidirectional solidification of Al–Si alloy, J. Mater. Process. Technol. 288 (2020) 116913, doi:10.1016/j.jmatprotec.2020.116913.
[41] H. Zhang, M. Wu, Y. Zheng, A. Ludwig, A. Kharicha, Numerical study of the role of mush permeability in the solidifying mushy zone under forced convection, Mater. Today Commun. 22 (2020) 100842, doi:10.1016/j.mtcomm.2019.100842.
[42] M. Ghods, L. Johnson, M. Lauer, R.N. Grugel, S.N. Tewari, D.R. Poirier, Radial macrosegregation and dendrite clustering in directionally solidified Al-7Si and Al-19Cu alloys, J. Cryst. Growth 441 (2016) 107–116, doi:10.1016/j.jcrysgro.2016.02.014.
[43] T. Wang, L. Hachani, Y. Fautrelle, Y. Delannoy, E. Wang, X. Wang, O. Budenkova, Numerical modeling of a benchmark experiment on equiaxed solidification of a Sn–Pb alloy with electromagnetic stirring and natural convection, Int. J. Heat Mass Transf. 151 (2020) 119414, doi:10.1016/j.ijheatmasstransfer.2020.119414.
[44] C.Y. Wang, C. Beckermann, Equiaxed dendritic solidification with convection: part II. Numerical simulations for an Al-4 Wt pet Cu alloy, Metall. Mater. Trans. A Phys. Metall. Mater. Sci. 27 (1996) 2765–2783, doi:10.1007/BF02652370.
[45] H. Combeau, M. Založnik, S. Hans, P.E. Richy, Prediction of macrosegregation in steel ingots: influence of the motion and the morphology of equiaxed grains, Metall. Mater. Trans. B Process Metall. Mater. Process. Sci. 40 (2009) 289–304, doi:10.1007/s11663-008-9178-y.
[46] A. Olmedilla, M. ZaloŽnik, B. Rouat, H. Combeau, Packing of sedimenting equiaxed dendrites, Phys. Rev. E. 97 (2018) 1–10, doi:10.1103/PhysRevE.97.012910.
[47] A. Olmedilla, M. ZaloŽnik, T. Messmer, B. Rouat, H. Combeau, Packing dynamics of spherical and nonconvex grains sedimenting at low Stokes number, Phys. Rev. E. 99 (2019) 1–11, doi:10.1103/PhysRevE.99.012907.
[48] A. Plotkowski, M.J.M. Krane, The effect of velocity based packing schemes on macrosegregation development in simulations of equiaxed solidification, Appl. Math. Model. 40 (2016) 9212–9227, doi:10.1016/j.apm.2016.05.031.
[49] A. Plotkowski, M.J.M. Krane, The discrete nature of grain attachment models in simulations of equiaxed solidification, Appl. Math. Model. 47 (2017) 31–44, doi:10.1016/j.apm.2017.03.009.
[50] M.C. Flemings, Behavior of metal alloys in the semisolid state, Metall. Trans. A. 22 (1991) 957–981, doi:10.1007/BF02661090.
[51] L. Arnberg, G. Chai, L. Backerud, Determination of dendritic coherency in solidifying melts by rheological measurements, Mater. Sci. Eng. A 173 (1993) 101–103, doi:10.1016/0921-5093(93)90195-K.
[52] G. Maymon, Some important statistical distributions, 2018. doi:10.1016/b978-0-12-814191-5.00002-4.
[53] D. Wang, L.S. Fan, Particle characterization and behavior relevant to fluidized bed combustion and gasification systems, 2013. 10.1533/9780857098801.1.42.
[54] E. Limpert, W.A. Stahel, M. Abbt, Log-normal distributions across the sciences: keys and clues, Bioscience 51 (2001) 341–352 10.1641/0006-3568(2001)051[0341:LNDATS]2.0.CO;2.
[55] T.E. Quested, A.L. Greer, P.S. Cooper, The variable potency of TiB_2 nucleant particles in the grain refinement of aluminium by Al-Ti-B additions, Mater. Sci. Forum. 396–402 (2002) 53–58, doi:10.4028/www.scientific.net/msf.396-402.53.